Journal of Colloid and Interface Science 384 (2012) 162–171

Contents lists available at SciVerse ScienceDirect

Journal of Colloid and Interface Science

www.elsevier.com/locate/jcis

Understanding anomalous current–voltage characteristics in microchannel–nanochannel interconnect devices

Vishal V.R. Nandigana, N.R. Aluru *

Department of Mechanical Science and Engineering, Beckman Institute for Advanced Science and Technology, University of Illinois at Urbana–Champaign, Urbana, IL 61801, USA

ARTICLE INFO

Article history:
Received 17 April 2012
Accepted 5 June 2012
Available online 15 June 2012

Keywords:
Micro–nanochannel
Concentration polarization
Space charge redistribution
Overlimiting current
AC/DC field
Current rectification

ABSTRACT

The integration of a microchannel with a nanochannel is known to exhibit anomalous nonlinear current–voltage characteristics. In this paper, we perform detailed numerical simulations considering a 2-D nonlinear ion transport model, to capture and explain the underlying physics behind the limiting resistance and the overlimiting current regions, observed predominantly in a highly ion-selective nanochannel. We attribute the overlimiting current characteristics to the redistribution of the space charges resulting in an anomalous enhancement in the ionic concentration of the electrolyte in the induced space charge region, beyond a critical voltage. The overlimiting current with constant conductivity is predicted even without considering the effects of fluidic nonlinearities. We extend our study and report anomalous rectification effects, resulting in an enhancement of current in the non-ohmic region, under the application of combined AC and DC electric fields. The necessary criteria to observe these enhancements and some useful scaling relations are discussed.

1. Introduction

Owing to the advancements in micro–nanomanufacturing technology, there is a significant interest to investigate the transport phenomenon in channel sizes of the order of few hundreds of nanometers [1–4]. Due to their large surface-area-to-volume ratio, the thickness of the electrical double layer (EDL) in these devices spans much of the channel height leading to the predominant transport of counterions in the channel. This enables the channel to be ion-selective [5], and hence can be used as an ion-exchange membrane. The transport in these devices is typically studied by connecting the nanochannel with two microchannels, and a potential difference is applied between the ends of the microchannel [6–9]. The integration of a micro- and a highly ion-selective nanochannel has paved way to many complex physics at the interfaces leading to anomalous effects in their transport [10].

Recent experiments by Kim et al. [11] and Yossifon et al. [12,13] revealed nonlinear current–voltage characteristics in a micro–nanochannel integrated system. The current characteristics were found to deviate from the classical diffusion-limited current transport theory [14], which predicts a saturation of the current density at higher applied voltages with an infinite differential resistance [14]. Fig. 1 shows a schematic illustration of the nonlinear current–voltage characteristics in a highly ion-selective nanochannel integrated with a microchannel. At low electric fields, the current increases linearly with the applied voltage, following the Ohm's law. This region is typically referred to as the Ohmic region or quasi-equilibrium region. However, beyond the first critical voltage (V_{LI}), the current deviates from the Ohmic behavior, but continues to increase with a slope smaller than that of the Ohmic region. This region is often referred to as the limiting resistance region (LRR). Finally, beyond a second critical voltage (V_{LII}), the slope of the current increases in comparison to the limiting regime, and this region is typically referred to as the overlimiting current region.

Many plausible mechanisms are discussed to explain the overlimiting current characteristics [15–17]. Using a 1-D ideal ion-selective membrane model, Rubinstein [18] suggested that the ionic concentration of the electrolyte does not saturate to zero at the depletion membrane surface, as predicted by the diffusion-limited theory. Further, Rubinstein et al. [19] predicted a region of induced space charge (SCR) between the quasi-equilibrium EDL and the electroneutral diffusion boundary layer (DBL) at the depletion junction, resulting in a decrease in the length of the DBL. This decrease in DBL length was believed to result in the overlimiting current. They further proposed a possible mechanism to select the length of the SCR, by measuring the thickness of the vortex array, developed due to the instabilities in the space charge region. Yossifon et al. [13] measured the vortex instability length from their experiments and used it as a parameter in their model, to capture the overlimiting current region in their nanoporous membrane. However, an exact physical understanding of the large, yet finite differential resistance in the limiting resistance region

* Corresponding author.
E-mail address: aluru@illinois.edu (N.R. Aluru).
URL: http://www.illinois.edu/~aluru (N.R. Aluru).

0021-9797/$ - see front matter © 2012 Elsevier Inc. All rights reserved.
http://dx.doi.org/10.1016/j.jcis.2012.06.004

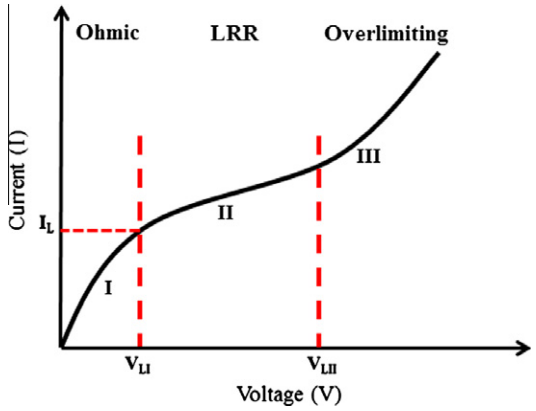

Fig. 1. Schematic illustration of nonlinear current–voltage characteristics of a typical ion-selective nanochannel integrated with a microchannel. LRR represents limiting resistance region.

and the transition from the limiting to the overlimiting region is still unclear. A comprehensive physical model to discuss all the three *I–V* regions by considering the micro–nanochannel interconnect system is still missing. In this paper, using a detailed 2-D nonlinear, non-ideal ion-selective model, we capture and explain all the three regions, by analyzing the behavior of the ionic concentration, near the depletion junction of the micro–nanochannel. The model predicts a constant conductivity in the overlimiting current region, which is consistent with the experimental results.

With the understanding of the polarization physics at the junctions of the micro–nanochannel, we investigate the influence of small-amplitude external AC perturbations along with the DC voltage, on the current characteristics, predominantly beyond the Ohmic region. The necessary criteria to observe the anomalous current rectification, resulting in an enhancement of current, under suitable AC field is discussed. Further, some useful scaling relations are presented. The anomalous transport characteristics may find applications in the field of water desalination, energy storage systems, protein separation, and in the field of supercapacitors.

The rest of the paper is outlined as follows. Section 2 discusses the nonlinear ion transport model. The necessary simulation details are elucidated in Section 3. A detailed discussion of the nonlinear current–voltage characteristics under the application of DC electric fields and under different EDL thickness is presented in Section 4. In Section 5, the anomalous rectification effect under combined AC/DC electric fields is discussed. Finally, conclusions are presented in Section 6.

2. Theory

2.1. Governing equations

In this section, the complete set of equations and the necessary boundary conditions to model the ion transport characteristics for a typical micro–nanochannel interconnect system (see Fig. 2) are discussed. It has been shown that an accurate description of ion transport can be provided using the concepts of continuum theory for dimensions larger than several nanometers [20,21,6]. Hence, continuum theory has been used in this paper, as the smallest dimension considered is 30 nm. In this study, we consider a symmetric monovalent electrolyte like *KCl* with bulk concentration, c_0, and assume that the concentration of H^+ and OH^- is much lower compared to the bulk concentration of the ionic species. Hence, the water dissociation effects are not considered in the numerical model [6]. Further, we assume that the ions inside the steric layer are rigidly held and do not contribute to the ionic current [20,22]. We also neglect the Faradaic reactions that occur near the electrode in the present study. Under these assumptions, the total flux of the ionic species is contributed by a diffusive component resulting from the concentration gradient, an electrophoretic component arising due to the potential gradient, and a convective component originating from the fluid flow. The total flux of each species in the solution is given by,

$$\mathbf{\Gamma}_i = -D_i \nabla c_i - \Omega_i z_i F c_i \nabla \phi + c_i \mathbf{u} \tag{1}$$

where $\mathbf{\Gamma}_i$ is the flux vector, F is Faraday's constant, z_i is the valence, D_i is the diffusion coefficient, Ω_i is the ionic mobility, c_i is the concentration of the ith species, $\mathbf{u}$ is the velocity vector of the fluid flow, and ϕ is the electrical potential. Note that the ionic mobility is related to the diffusion coefficient by Einstein's relation [14], $\Omega_i = \frac{D_i}{RT}$, where R is the ideal gas constant and T is the thermodynamic temperature. The mass transfer of each buffer species is given by,

$$\frac{\partial c_i}{\partial t} = -\nabla \cdot \mathbf{\Gamma}_i \tag{2}$$

The individual ionic current through the channel is calculated by integrating their respective fluxes over the cross-sectional area, i.e.,

$$\mathbf{I}_i = \int_S z_i F \mathbf{\Gamma}_i \, dS \tag{3}$$

and the total ionic current through the channel is calculated as,

$$\mathbf{I} = \int_S \sum_i z_i F \mathbf{\Gamma}_i \, dS \tag{4}$$

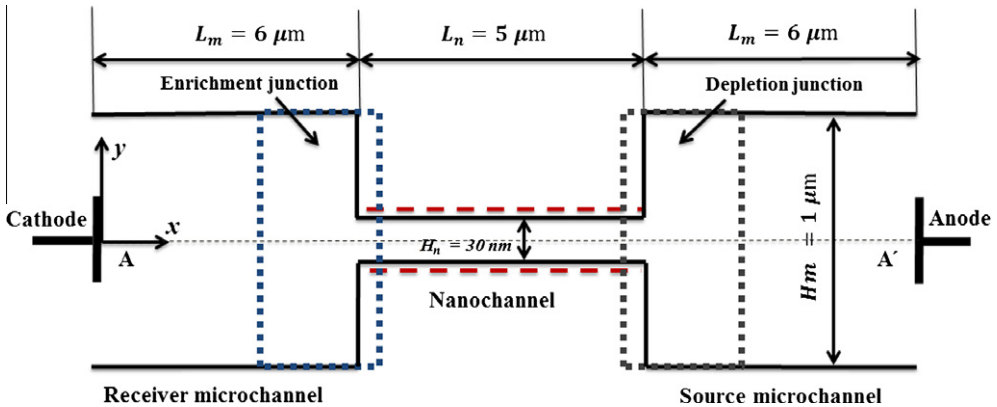

Fig. 2. Simulation set-up (not drawn to scale), consisting of a negatively charged nanochannel connected to two microchannels.

where S is the cross-sectional area of the channel. The electrical potential distribution is calculated by solving the Poisson equation,

$$\nabla \cdot (\epsilon_r \nabla \phi) = -\frac{\rho_e}{\epsilon_0} \tag{5}$$

where ϵ_0 is the permittivity of free space, ϵ_r is the relative permittivity of the medium, and ρ_e is the net space charge density of the ions defined as,

$$\rho_e = F\left(\sum_{i=1}^{m} z_i c_i\right) \tag{6}$$

where m is the total number of species considered in the system. Eq. (5), Eqs. (2), and (1) are the classical Poisson–Nernst–Planck (PNP) equations, which describe the electrochemical transport. The incompressible Navier–Stokes and the continuity equations are considered, to describe the movement of the fluid flow,

$$\rho\left(\frac{\partial \mathbf{u}}{\partial t} + \mathbf{u} \cdot \nabla \mathbf{u}\right) = -\nabla p + \mu \nabla^2 \mathbf{u} + \rho_e \mathbf{E} \tag{7}$$

$$\nabla \cdot \mathbf{u} = 0 \tag{8}$$

where p is the pressure, ρ and μ are the density and the viscosity of the fluid, respectively, and $\mathbf{E} = -\nabla\phi$ is the electric field. $\rho_e \mathbf{E}$ is the electrostatic body force acting on the fluid due to the space charge density and the applied electric field. The aforementioned set of coupled PNP and Navier–Stokes equations are also referred to as the space charge model [23,24].

We discuss the necessary boundary conditions for the closure of the problem. The normal flux of each ion is assumed to be zero [25] on all the channel walls, so that there is no leakage of current. The fluid velocity on the wall surfaces is assumed to be subjected to non-slip boundary condition, and the gradients of pressure are assumed to be zero on the walls. Applying the charge conservation at the walls lead to the following electrostatic boundary condition,

$$\mathbf{n} \cdot \nabla \phi = \frac{\sigma}{\epsilon_0 \epsilon_r} \tag{9}$$

where $\mathbf{n}$ denotes the unit normal vector (pointing outwards) to the wall surface and σ is the surface charge density of the walls. We consider the microchannel on the right side as the source and is given a positive voltage (ϕ^{DC}), while, the microchannel on the left is considered as the receiver and is grounded. The boundary conditions at the ends of the source (Eq. (10)) and receiver (Eq. (11)) microchannels are specified as:

$$\phi = \phi^{DC}, \quad c_i = c_o, \quad \mathbf{n} \cdot \nabla \mathbf{u} = 0, \quad p = 0 \tag{10}$$

$$\phi = 0, \quad c_i = c_o, \quad \mathbf{n} \cdot \nabla \mathbf{u} = 0, \quad p = 0 \tag{11}$$

All the equations are non-dimensionalized by scaling the distance with the length of the microchannel (L_m), time with the diffusion time scale (L_m^2/D), concentration with the bulk concentration of the electrolyte solution (c_0), electric potential with $\phi_0 = RT/Fz$, fluid velocity with $U_0 = \epsilon_0 \epsilon_r E_0 \phi_0 / \mu$, where E_0 is the average applied field in the system, pressure with $p_0 = \mu U_0 / L_m$, and space charge density with $\rho_{e_0} = Fzc_0$. We consider a symmetric monovalent electrolyte ($z_+ = -z_- = z$) like KCl in the present analysis and normalize the diffusion coefficient of each ionic species with the characteristic diffusion coefficient, $D = 2 \times 10^{-9}$ m^2/s. Applying these scaling variables, the system of governing equations in the dimensionless form can be written as:

Transport of positive ions,

$$\frac{\partial c_+^*}{\partial t^*} = D_+^* \nabla^{*2} c_+^* + D_+^* \nabla^* \cdot (c_+^* \nabla^* \phi^*) - Pe \nabla^* \cdot (c_+^* \mathbf{u}^*) \tag{12}$$

Transport of negative ions,

$$\frac{\partial c_-^*}{\partial t^*} = D_-^* \nabla^{*2} c_-^* - D_-^* \nabla^* \cdot (c_-^* \nabla^* \phi^*) - Pe \nabla^* \cdot (c_-^* \mathbf{u}^*) \tag{13}$$

Poisson equation for electrical potential,

$$\nabla^{*2} \phi^* = -\frac{1}{2\beta^2} \rho_e^* \tag{14}$$

Conservation of mass

$$\nabla^* \cdot \mathbf{u}^* = 0 \tag{15}$$

Conservation of momentum

$$\frac{1}{Sc} \frac{\partial \mathbf{u}^*}{\partial t^*} + Re\, \mathbf{u}^* \cdot \nabla^* \mathbf{u}^* = -\nabla^* p^* + \nabla^{*2} \mathbf{u}^* + \frac{1}{2\beta^2} \rho_e^* \mathbf{E}^* \tag{16}$$

In the above equations, variables with superscript '$*$' are the dimensionless variables. The various non-dimensional numbers are given by, $\beta = \lambda_D / L_m$, Peclet number, $Pe = L_m U_0 / D$, Reynolds number, $Re = \rho U_0 L_m / \mu$, and Schmidt number, $Sc = \nu / D$ is the ratio of the kinematic viscosity ($\nu = \mu/\rho$) to the ionic diffusion coefficient. The Debye length (λ_D), determining the thickness of the EDL, is defined as, $\lambda_D = \sqrt{\epsilon_0 \epsilon_r RT / 2F^2 z^2 c_0}$. In the present study, we understand the current–voltage characteristics for different values of β. Typically, β varies in the range of $10^{-3} - 10^{-5}$ [13].

Using the aforementioned set of equations, analytical expressions are derived (see Appendix for details) to calculate the magnitude of the normalized limiting current per unit width ($I_L^* = |I_L / FzDc_0|$) and the corresponding normalized first critical voltage ($V_{LI}^* = V_{LI} Fz / RT$). These expressions provide a quick understanding of the effect of the micro–nanochannel geometry and each system parameter on the emergence of nonlinear effects, i.e.,

$$I_L^* = \frac{2H_m}{L_m}\left(\frac{\hat{c}_{n+} + \hat{c}_{n-}}{\hat{c}_{n+} - \hat{c}_{n-}}\right) \tag{17}$$

$$V_{LI}^* = -I_L\left(\frac{L_n}{FzDH_n(\hat{c}_{n+} + \hat{c}_{n-})}\right) + ln\left(\frac{\hat{c}_+|_{x=x_{e^-}}}{\hat{c}_+|_{x=x_{e^+}}}\right) - I_L\left(\frac{L_m}{FzDH_m c_0}\right) \tag{18}$$

where $\hat{c}_{n+}$ and $\hat{c}_{n-}$ are the counter-ion and co-ion concentration inside the nanochannel (averaged over the height of the nanochannel, H_n). $\hat{c}_+|_{x=x_{e^-}}$ and $\hat{c}_+|_{x=x_{e^+}}$ are the cation concentration (averaged over the channel height) at the left and right end of the anodic micro–nanochannel interface, respectively (see Fig. A.1 and Appendix for details). L_n and H_m are the nanochannel length and microchannel height, respectively. It can be observed from Eq. (17) that, in the case of an ideal cation-selective membrane, ($\hat{c}_{n-} = 0$), we obtain the classical asymptotic limit given by the diffusion-limited theory, $I_L^*|_{ideal} = \frac{2H_m}{L_m}$ [26], for a symmetric monovalent electrolyte.

3. Simulation details

The simulated domain consists of a rectangular nanochannel of length 5 μm (L_n) and height 30 nm (H_n) connected to two microchannels of length 6 μm (L_m) and height 1 μm (H_m), on either side of the nanochannel (see Fig. 2). A $2-D$ simulation study is carried out by assuming that the depth (perpendicular to the plane of the paper) of the micro- and nanochannel to be much larger than the length. The operating temperature is $T = 300$ K, the density and the viscosity of the fluid are 1000 kg/m^3 and 1.003×10^{-3} Pa · s, respectively. The diffusivities of K^+ and Cl^- are 1.96×10^{-9} m^2/s and 2.03×10^{-9} m^2/s, respectively. We assume the dielectric constant of the aqueous solution to be $\epsilon_r = 80$ [27]. Further, we also assume the surface charge on the walls of the microchannel $\sigma_m = 0$ and on nanochannel, $\sigma_n = -1$ mC/m^2, respectively (Ref. [28,29] for details).

The coupled PNP and Navier–Stokes equations are numerically solved using the finite volume method in OpenFOAM [30] (Open Field Operation and Manipulation). The convective terms in the

PNP equations are discretized using second-order bounded NVD schemes [31], and all the Laplacian terms are discretized using second-order central differencing scheme. SIMPLE algorithm is used for pressure–velocity coupling [32]. Second-order implicit time-differencing scheme [30] is used to discretize the variables in time. A finer mesh is introduced near the walls, at the entrance, and exit of the nanochannel. The model is validated with the numerical results of Daiguji et al. [20,21] and Jin et al. [6] (refer [29] for full details). Furthermore, the results reported here are ensured to be independent of the grid size.

4. Results and discussion

4.1. Nonlinear current–voltage characteristics

We initially consider low bulk ionic concentration, $c_0 = 0.1$ mM (corresponding to a thick EDL regime, $\beta = 0.0051$) to investigate the current–voltage characteristics. As mentioned in our previous study [28], the nanochannel ion selectivity can be modulated by controlling the bulk ionic concentration (in other words controlling λ_D) and also by controlling the nanochannel wall surface charge density. In this study, we use the former approach to control the ion-selectivity, and the study can easily be extended to understand the surface charge effects. Fig. 3 shows the magnitude of the normalized current as a function of the normalized voltage which reveals all the three regions, namely Ohmic region, limiting resistance region (LRR), and the overlimiting region. In this section, we will briefly discuss the first two regions. In the Ohmic/quasi-equilibrium region, the current is found to vary linearly with the applied voltage. With increase in the voltage, the current deviates from the Ohmic behavior as shown in the inset of Fig. 3. The normalized value of I_L (in magnitude) and the first critical voltage, V_{LI}, are found to be 0.3175 and 13.5394, respectively. The corresponding analytical values (using Eq. (17) and Eq. (18)) are 0.347 and 13.8205, respectively. The analytical expressions provide a reasonable degree of accuracy in comparison to the numerical solutions. Fig. 3 also reveals that the current beyond the first critical voltage does not saturate as predicted by the classical diffusion-limited theory, but increases with a slope smaller than that of the Ohmic region. All these results are consistent with the experiments of Yossifon et al. [13] and Kim et al. [11] for a micro–nanochannel system.

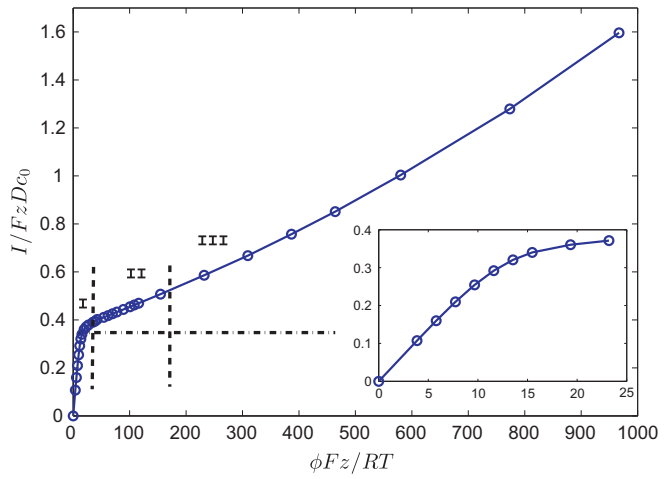

Fig. 3. Normalized current–voltage characteristics (in magnitude) of a cation-selective nanochannel connected to two microchannels. The dashed dotted line shows the analytical value of the limiting current. Region I corresponds to the Ohmic region, II represents the limiting resistance region (LRR), and region III corresponds to the overlimiting region. The inset of the figure displays the transition from the Ohmic region to the limiting resistance region.

An exact reason for the large, yet finite differential resistance in the limiting resistance region is yet to be understood in these systems [13]. In order to understand this, we investigate the ionic concentration distribution along the axial direction in the Ohmic region and in the LRR. Fig. 4a shows that, for DC voltage ($\phi^{DC}Fz/RT = 7.7367$), corresponding to the Ohmic region, due to the concentration polarization effects, there is a depletion of ions in the anodic region and an enrichment of ions in the cathodic region [10]. This results in a linear concentration gradient from the end of the microchannel (where the concentration of the ionic solution is the bulk ionic concentration) until the regions close to the micro–nanochannel interface. We also observe that local electroneutrality is maintained in the regions of linear concentration gradient, with no additional space charges. Typically, these regions are referred to as the diffusion boundary layer (DBL) regions [18]. It is also observed that the linear concentration gradient in the DBL regions becomes steeper with the increase in the voltage. Further, we observe a thin quasi-equilibrium EDL region at the micro/nanochannel depletion interface (see inset of Fig. 4a). Similarly, we also observe a thin quasi-equilibrium EDL region at the micro/nanochannel enrichment interface. Furthermore, Fig. 4 reveals that, in the Ohmic region, the location of the minimum anion

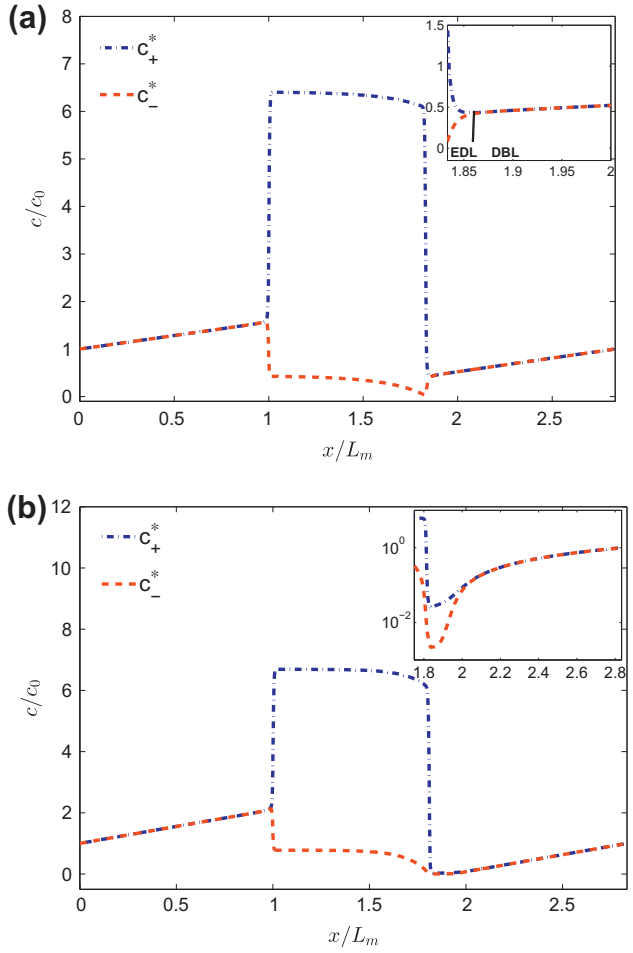

Fig. 4. (a) Normalized ionic concentration along the axial direction, for $\phi^{DC}Fz/RT = 7.7367$, corresponding to the Ohmic region. The inset of the figure shows the thin quasi-equilibrium EDL region at the depletion micro/nanochannel interface. (b) Normalized ionic concentration along the axial direction, for $\phi^{DC}Fz/RT = 77.3677$, corresponding to the limiting resistance region. The inset of the figure shows the nonlinear concentration distribution due to the presence of induced space charges near the micro–nanochannel depletion interface. In all these cases, $\beta = 0.0051$.

concentration is inside the nanochannel. The minimum anion concentration along the axial direction is observed at $x/L_m = 1.8267$.

Fig. 4b shows that, for DC voltage ($\phi^{DC}Fz/RT = 77.3677$), corresponding to the limiting resistance region, the ionic concentration at the depletion micro/nanochannel interface does not saturate to zero as predicted by the classical diffusion-limited theory. Further, a region of space charge is induced between the quasi-equilibrium EDL at the micro–nanochannel depletion interface and the local electroneutral diffusion boundary layer. The induced space charge region results in a nonlinear concentration distribution near the depletion interface (see inset of Fig. 4b). Further, we observe that, beyond the first critical voltage, the location of the minimum anion concentration shifts from the nanochannel region toward the microchannel interface region. The new location of the minimum anion concentration along the axial direction is observed at $x/L_m = 1.8375$, which is outside the nanochannel. It is also found that the new position of the minimum anion concentration does not change beyond the first critical voltage. In spite of the changes in the concentration near the depletion junction, we observe that a linear concentration gradient and local electroneutrality are always maintained in the cathodic enrichment region.

Fig. 5 shows the resistance of each channel as a function of DC voltage. The normalized resistance in each channel is numerically determined by calculating the normalized voltage drop across each channel and dividing it with the magnitude of the normalized current. It can be observed that, in the Ohmic region, the nanochannel has a constant finite conductance, and hence should be considered in understanding the current characteristics in such interconnect systems unlike most of the earlier theories discussed in the literature [15,18]. The large nanochannel resistance can be understood from the fact that most of the voltage drop occurs inside the nanochannel in the Ohmic region. Further, the inset of Fig. 5 shows that the resistance of the depletion microchannel is relatively smaller compared to the nanochannel resistance. This is because we observe that the microchannel is still electroneutral, even though there is a depletion of ions. Furthermore, in the enrichment microchannel, as the concentration of the ionic species is greater than the bulk ionic concentration, the resistance of this microchannel is minimal.

In the limiting resistance region (LRR), Fig. 5 reveals that there is a gradual increase in the resistance of the depletion microchannel, and it starts becoming comparable to the nanochannel resistance as the voltage increases. This is due to the formation of the induced space charges near the depletion micro/nanochannel interface resulting in an increase in the electric field at this interface. Hence, beyond the Ohmic region, the resistance of both the nanochannel and the depletion microchannel is important. Furthermore, we note that the induced space charge is accompanied by a shift in the location of the minimum anion concentration toward the microchannel interface. Fig. 6a and b reveal the normalized ionic concentration along the axial direction for various DC electric fields ($\phi^{DC}Fz/RT = 77.3677, \phi^{DC}Fz/RT = 116.0516, \phi^{DC}Fz/RT = 232.1032, \phi^{DC}Fz/RT = 773.6773$), beyond the first critical voltage. It can be observed that, until the second critical voltage, the charges propagate predominantly toward the anodic end of the microchannel. This is accompanied by a monotonic decrease in the minimum anion concentration as shown in Fig. 7. We believe that the predominant propagation of charges toward the microchannel along with the decrease in the minimum anion concentration until the second critical voltage, results in a finite differential resistance. Hence, we observe a change in the slope of the *I–V* curve, leading to the limiting resistance region. The anomalous increase in the minimum anion concentration beyond the second critical voltage (see Fig. 7) leading to the overlimiting current would be discussed in the next section.

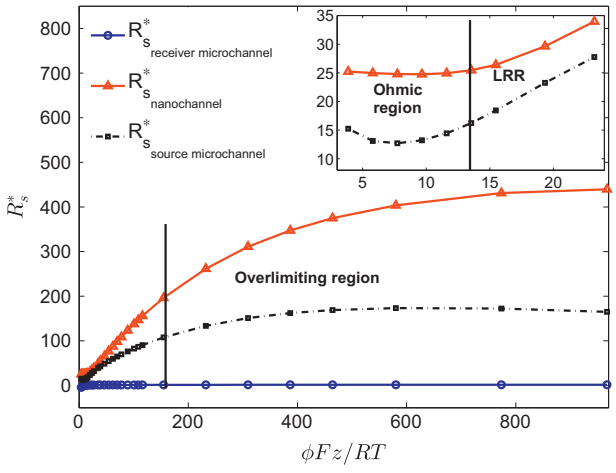

Fig. 5. Variation of the normalized resistance as a function of the normalized DC voltage in different regions of the system. The bold line indicates the transition to the overlimiting region. The inset of the figure shows the variation of the normalized resistance in the Ohmic and limiting resistance region.

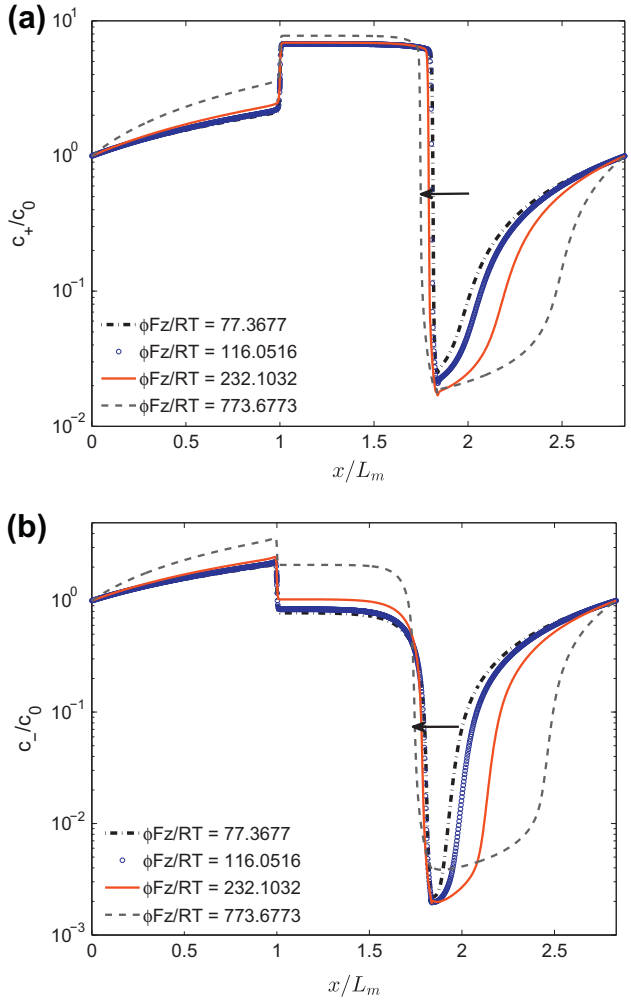

Fig. 6. Normalized concentration along the axial direction of (a) cations (counterions) and (b) anions (co-ions) for various DC voltages, corresponding to the limiting resistance and overlimiting region. The solid arrow shows that the induced space charge region, formed near the depletion source microchannel–nanochannel interface, propagates inside the nanochannel region under a large DC voltage, $\phi^{DC}Fz/RT = 773.6773$, corresponding to the overlimiting region.

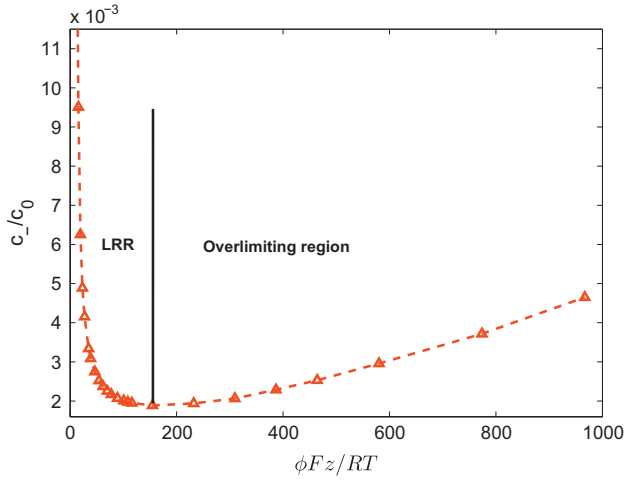

Fig. 7. Variation of the minimum anion concentration (normalized) near the micro–nanochannel depletion interface for various normalized applied DC voltages corresponding to the limiting resistance (LRR) and overlimiting regions, respectively.

4.2. Overlimiting current characteristics

Fig. 3 shows that beyond a second critical voltage ($V^*_{LII} = 154.7355$), the slope of the *I–V* curve increases from that of the limiting region leading to the overlimiting current region. Fig. 6a and b show that, beyond the second critical voltage, the space charges formed near the depletion junction propagate inside the nanochannel (solid arrow indicates the propagation of charges inside the nanochannel) along with its propagation toward the anodic end of the microchannel. Such propagation of space charges under large DC electric fields can be captured only by considering the entire micro–nanochannel interconnect system. The propagation leads to a redistribution of space charge near the depletion interface, resulting in an increase in the concentration of the ions near this interface as shown in Fig. 6a and b. Further, we observe that the increase in the concentration is more pronounced in the case of anions (co-ion) compared to that of the cation (counter-ion) concentration. Furthermore, the propagation of charges toward the nanochannel interface results in a significantly higher electric field inside the nanochannel interface beyond the second critical voltage. These effects result in a shift in the slope of the overall system resistance beyond the second critical voltage (see Fig. 5), leading to an overlimiting current region. We note that, by investigating the behavior of the minimum anion concentration alone, we can capture all the three regions of the *I–V* characteristics.

We would also like to highlight that all the three regions of the *I–V* curve can be captured and explained even without considering the fluid flow equations in the model (see Fig. 8). This suggests that the fluidic nonlinearities observed in the space charge region may not necessarily contribute toward understanding the origin of the overlimiting current. Fig. 8 also shows the current characteristics at high concentration limit, $c_0 = 5$ mM, corresponding to thin EDL regime ($\beta = 7.2605 \times 10^{-4}$). Under thin EDL limit, the ion selectivity of the nanochannel decreases significantly and we do not observe the space charges at the depletion region. Hence, we observe only Ohmic region in the current–voltage characteristics. Thus, the ion-selectivity of the nanochannel plays a prominent role in order to observe all the three regions of the *I–V* curve.

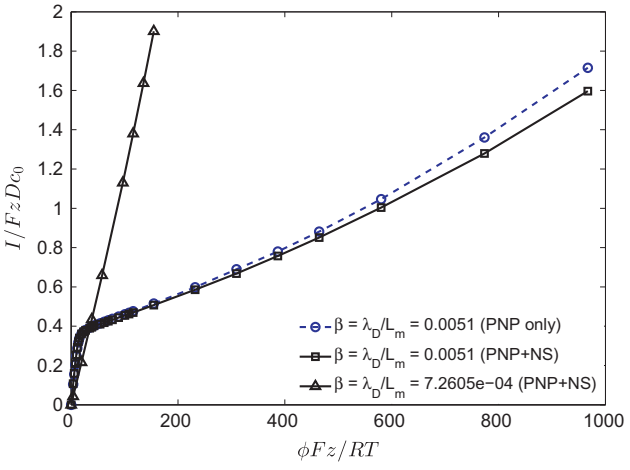

Fig. 8. Effect of dimensionless EDL thickness ($\beta = \lambda_D/L_m$) on the normalized current–voltage characteristics (in magnitude). Here, β is varied by changing the bulk ionic concentration (c_0) of the electrolyte.

5. Anomalous current rectification under combined AC/DC electric fields

We extend our study to investigate the influence of small-amplitude external AC perturbations along with the DC voltage on the current characteristics. Note that the application of a large AC amplitude leads to higher complexities in the system, which is beyond the scope of the present work. In order to understand the AC effects, we solve the same set of governing equations with the necessary boundary conditions discussed in Section 3. The only variation is the boundary condition for the potential at the source microchannel,

$$\phi = \phi^{DC} + \phi^{AC} sin(\omega t) \tag{19}$$

where ϕ^{AC} is the amplitude of the AC electric potential and ω is the angular frequency ($\omega = 2\pi f$, f is the applied frequency). An AC voltage is applied after the system reaches a steady-state with the DC field. We consider the same system parameters as discussed before and initially investigate the effect of combined AC/DC electric fields under thick EDL limit ($\beta = 0.0051$). We understand the frequency effects using the dimensionless frequency (fL_m^2/D) and consider the ratio of AC amplitude to DC voltage ($\alpha = \phi^{AC}/\phi^{DC}$) to investigate the amplitude effects. Further, the effect of the combined AC/DC electric field on the current characteristics is investigated by time-averaging the current (per unit width) measured at the end of the source microchannel over one time period:

$$\langle \mathbf{I} \rangle = \frac{1}{T_p} \int_0^{T_p} \mathbf{I}\, dt \tag{20}$$

where T_p is the time period of one cycle. In Fig. 9, we present the relative current rectification as a function of the dimensionless frequency (fL_m^2/D) for various DC voltages. To understand the frequency effects, α (= 1.333) is kept constant. The relative current rectification is calculated as:

$$\frac{\Delta \mathbf{I}}{\mathbf{I}_{DC}} = \frac{\langle \mathbf{I} \rangle - \mathbf{I}_{DC}}{\mathbf{I}_{DC}} \tag{21}$$

where $\mathbf{I}_{DC}$ is the current (per unit width) obtained when only DC voltage is applied and $\langle \mathbf{I} \rangle$ is the time-averaged current (per unit width) under combined AC/DC electric field computed using Eq. (20). It can be observed that for a given DC voltage of $\phi^{DC} Fz/RT = 77.3677$, at a low frequency, ($fL_m^2/D = 90$), there is no significant current rectification. However, with increase in the frequency, positive rectification effects are observed with enhancements in the current. A maximum positive current rectification is observed at $fL_m^2/D = 540$, while a further increase in the frequency

leads to a decrease in the rectification effects. Furthermore, at a very high frequency ($fL_m^2/D = 4500$), no current rectification is observed. Similar anomalous rectification effects were also observed in the experiments of Rubinstein et al. [18,33] for simple cation-selective ion-exchange membranes. Fig. 9 also shows that as the DC voltage increases and under same α, the rectification effects increase. Furthermore, we observe that, for a given system, the frequency at which the maximum positive rectification occurs is independent of the applied DC voltage, provided the voltage is beyond the first critical voltage.

In order to understand the current rectification, we consider a 1-*D* Nernst–Planck (NP) model and investigate the current (per unit width) in the induced space charge region using Eq. (1) and Eq. (4). Neglecting the contributions of diffusive and convective flux in the induced space charge region, and assuming a symmetric monovalent electrolyte with equal diffusivities ($D_+ = D_- = D$), we obtain the following expression for the total current per unit width,

$$I = -\frac{F^2 z^2 D H_m}{RT}\frac{d\hat{\phi}}{dx}(\hat{c}_+ + \hat{c}_-) \tag{22}$$

where $\wedge$ denotes the area-averaged quantity considering the width of the system to be unity. Under the application of combined AC and DC field, we assume, $(\hat{c}_+ + \hat{c}_-) = C_0 + C_1 cos(\omega t + \theta_1)$ and $\frac{d\hat{\phi}}{dx} = \phi_{x_0} + \phi_{x_1} cos(\omega t + \phi_1)$, neglecting the contribution of other higher harmonic components. C_0, ϕ_{x_0} are the DC component of the total ionic concentration and the field, respectively. C_1, ϕ_{x_1} are the respective first harmonic contributions of the ionic concentration and field. θ_1 and ϕ_1 are the corresponding phase angles of the former and latter terms, respectively. Substituting the aforementioned expressions into Eq. (22) and averaging over one time period (T_p), the time-averaged current per unit width $\langle I \rangle$ due to the combined AC and DC electric field is calculated as,

$$\langle I \rangle = I_{DC} - \frac{F^2 z^2 D H_m}{RT}\frac{C_1 \phi_{x_1}}{2} cos(\theta_1 - \phi_1) \tag{23}$$

where $I_{DC} = -\frac{F^2 z^2 D H_m}{RT}(C_0 \phi_{x_0})$ is the DC component of the current per unit width. To explain the current rectification under different excitation frequencies, the normalized first harmonic contribution of the total concentration and field, ($C_1^* \phi_{x_1}^* = C_1 \phi_{x_1} L_m / c_0 \phi_0$), and their relative phase difference $(\theta_1 - \phi_1)$ is numerically calculated in the induced space charge region at $x/L_m = 2$, for a given DC voltage of $\phi^{DC} Fz/RT = 154.7354$. The results are shown in Fig. 10. It can be observed that for low frequency, inspite of large contribution of the harmonic terms, we do not observe significant rectification as the electric field and the ionic concentration tend to be out of phase with each other $(\theta_1 - \phi_1 \simeq 90^\circ)$ as shown in the inset of Fig. 10, while, at a very high frequency ($fL_m^2/D = 4500$), we observe minimal contribution from the harmonic terms ($C_1^* \phi_{x_1}^* \simeq 0$) (see Fig. 10), and hence observe minimal rectification. However, at moderate excitation frequencies, we observe an appreciable contribution of the ionic concentration and the electric field. Also at these frequencies, the relative phase difference between the concentration, C_1^* and field, $\phi_{x_1}^*$ decreases, which implies that they gradually tend to become in-phase with each other as shown in the inset of Fig. 10. The above two effects together result in a positive current rectification, and a maximum rectification is observed at $fL_m^2/D = 540$. These arguments also help us to conclude that the current rectification can be understood without considering the effects of fluidic nonlinearities observed in the induced space charge region of micro/nanochannel as we have neglected the convective flux contribution in the $1-D$ NP model. Similar physics is also observed at other DC voltages, beyond the first critical voltage. Furthermore, from our NP model, we would like to comment that it is also possible to suppress the current and achieve negative rectification under combined AC/DC electric field when $fL_m^2/D \leqslant 1$, as the relative phase difference between the concentration and field $(\theta_1 - \phi_1)$can be greater than 90°.

Fig. 9 also shows that, when the DC voltage is in the Ohmic regime ($\phi^{DC} Fz/RT = 7.7367$), that is, when there are no induced space charges near the depletion micro–nanochannel interface, no change in the time-averaged current is observed at any frequency, under same α. These results are observed due to the minimal contribution of the harmonic terms $(C_1 \phi_{x1})$ to the DC current. Thus, the application of combined AC/DC electric fields offer a means to control the current beyond the Ohmic region. Further, the combined AC/DC electric field can also be potentially used to understand and measure the induced space charge region developed at the depletion micro/nanochannel interface. Fig. 11 displays the relative current rectification as a function of α. To understand the amplitude effects, the frequency ($fL_m^2/D = 450$) and DC voltage, $\phi^{DC} Fz/RT = 154.7354$, are kept constant. It is observed that the relative rectification shows a quadratic scaling with α.

5.1. EDL effects on AC current rectification

In this section, we understand the AC current rectification for different EDL thickness, $\beta = \lambda_D/L_m$. β is varied by changing the bulk

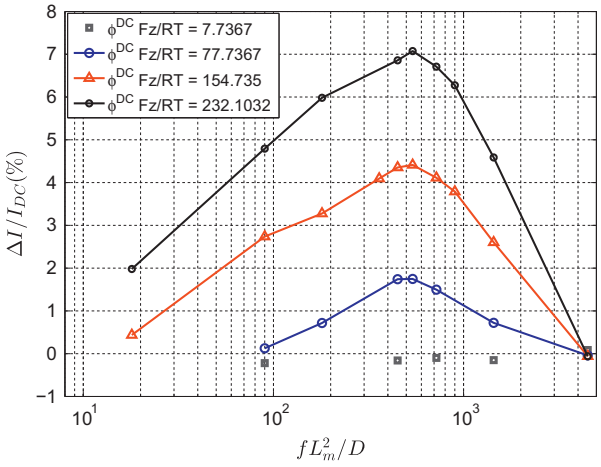

Fig. 9. Relative current rectification as a function of non-dimensional frequency (fL_m^2/D) for various DC voltages, at a constant $\alpha = \phi^{AC}/\phi^{DC} = 1.333$ and β = 0.0051.

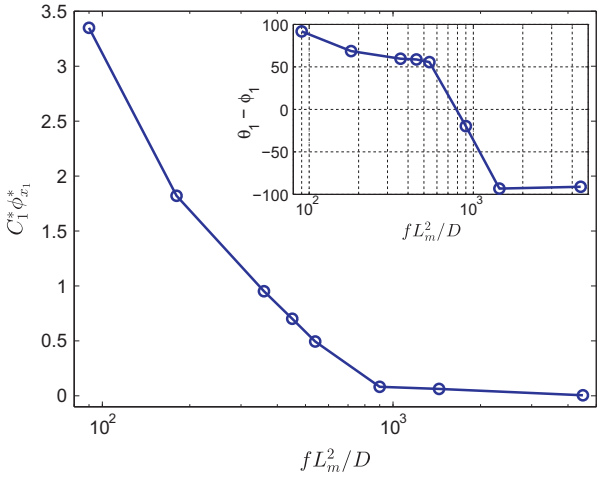

Fig. 10. Numerically calculated normalized first harmonic contribution of total ionic concentration and field, $(C_1^* \phi_{x_1}^*)$ in the induced space charge region at $x/L_m = 2$, as a function of non-dimensional frequency (fL_m^2/D), at a constant DC voltage $\phi^{DC} Fz/RT = 154.7354, \alpha = 1.333$ and $\beta = 0.0051$. The inset of the figure shows the relative phase angle between C_1^* and $\phi_{x_1}^*$ as a function of non-dimensional frequency.

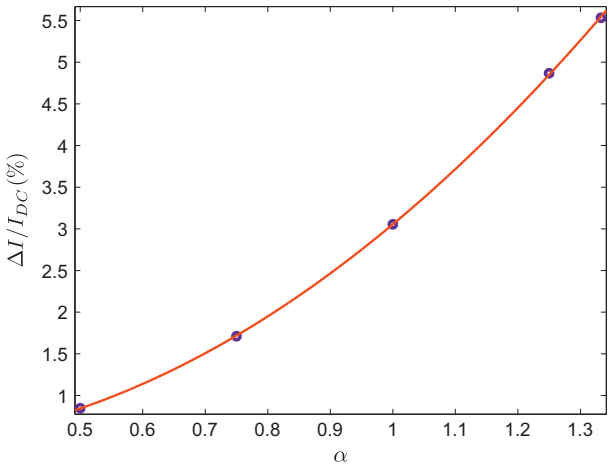

Fig. 11. Relative current rectification as a function of α at a constant DC voltage, $\phi^{DC}Fz/RT = 154.7354$, $fL_m^2/D = 450$ and $\beta = 0.0051$.

Table 1
Bulk concentration (c_0) and corresponding dimensionless EDL thickness.

c_0 (mM)	λ_D (nm)	β ($\times 10^{-3}$)
0.06	39.768	6.628
0.1	30.804	5.134
0.2	21.782	3.630
0.333	16.880	2.813

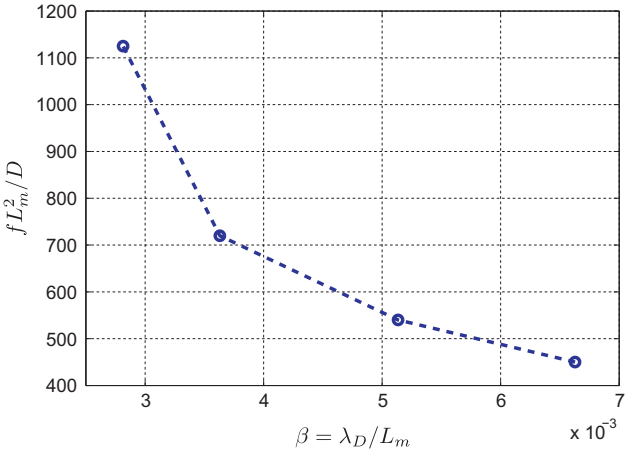

Fig. 12. Dimensionless frequency (at which positive current rectification is maximum) as a function of non-dimensional EDL thickness (β) at a fixed DC voltage, $\phi^{DC}Fz/RT = 154.7354$ and $\alpha = 1.333$.

ionic concentration (c_0) of the electrolyte. The bulk ionic concentrations chosen are summarized in Table 1. Note that a similar range of low ionic concentrations are used even in experiments on highly ion-selective nanochannels [13]. For each concentration, different AC frequencies are applied systematically to understand the current rectification. Fig. 12 shows the dimensionless frequency, at which the current rectification is maximum, as a function of β at a constant amplitude ($\alpha = 1.333$) and DC voltage, $\phi^{DC}Fz/RT = 154.7354$. The applied DC voltage is ensured to be greater than the first critical voltage, V_{LI}, for all the concentration cases chosen. We observe that the dimensionless frequency approximately scales inversely with β.

Fig. 13 shows the AC current rectification as a function of dimensionless frequency, under two different EDL limits, $\beta = 0.0051$, corresponding to thick EDL region (when the nanochannel is highly ion-selective) and $\beta = 7.2605 \times 10^{-4}$, corresponding to thin EDL limit, that is, when the ion-selectivity of the nanochannel is significantly reduced. Here, amplitude ($\alpha = 1.333$) and DC voltage, $\phi^{DC}Fz/RT = 154.7354$, are kept constant. Under thin EDL limit, minimal current rectification is observed, as the induced space charge region is not developed at the depletion micro–nanochannel interface. As discussed in Section 5, we observe only the Ohmic region in the absence of induced space charge region (see Fig. 8). The minimal current rectification at thin EDL limit further reveals the criteria to establish positive current rectification phenomenon.

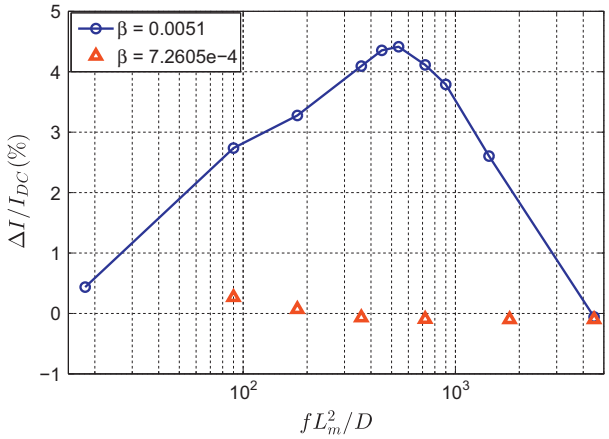

Fig. 13. Effect of dimensionless EDL thickness (β) and non-dimensional frequency (fL_m^2/D) on relative current rectification at a constant DC voltage, $\phi^{DC}Fz/RT = 154.7354$ and $\alpha = 1.333$.

6. Conclusions

Using a detailed 2-D nonlinear ion transport model, the large yet finite differential resistance in the limiting resistance region and the transition to the overlimiting current region are explained. The regions are distinguished by analyzing the propagation of space charges and the behavior of the ionic concentration in the induced space charge region, developed at the depletion micro–nanochannel junction. The overlimiting current is predicted even without considering the effects of fluidic nonlinearities near the depletion junction. Furthermore, anomalous current rectification, resulting in an enhancement of the current, under combined AC/DC electric field is discussed. The necessary criteria to observe these rectification effects and some useful scaling relations are presented. We believe the application of combined AC/DC electric field can offer a control on the current in the limiting resistance region and can also be potentially used to understand and measure the space charge region, induced near the depletion micro–nanochannel interface. The anomalous current characteristics may also find applications in the field of energy storage systems, supercapacitors, water desalination, and selective species separation.

Acknowledgments

This work was supported by the National Science Foundation (NSF) under Grants 0328162 (nano-CEMMS, UIUC), 0852657, 0915718, and 0941497. The authors thank Dr. X. Jin for helpful discussions. The authors gratefully acknowledge the use of the parallel computing resource provided by the University of Illinois.

Appendix A. Derivation of limiting current and first critical voltage

We use an approach similar to Yossifon et al. [13] and Manzanares et al. [34], to calculate the limiting current, I_L per unit width.

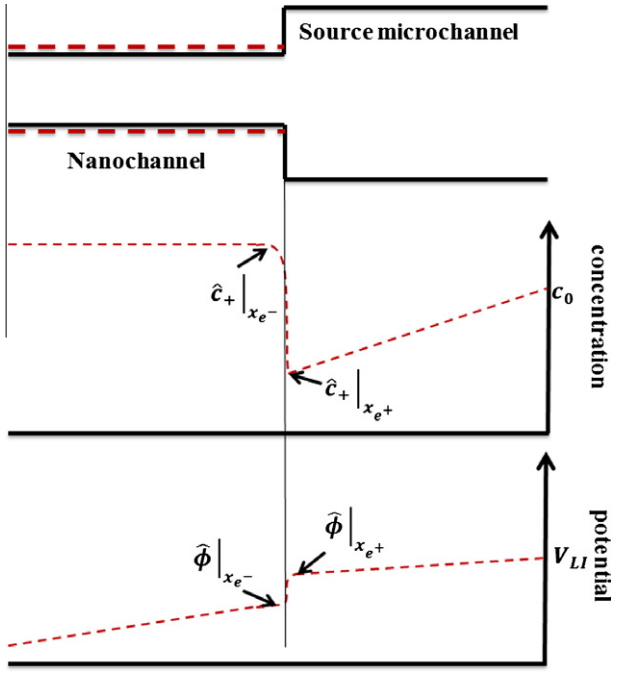

Fig. A.1. Schematic representation of a cation-selective nanochannel (top) illustrating the cation concentration (middle) and potential distribution (bottom) near the anodic micro–nanochannel interface under the application of first critical voltage, which results in the appearance of the limiting resistance region.

Using a $1-D$ model, and assuming a symmetric monovalent electrolyte, with equal diffusivities ($D_+ = D_- = D$) and neglecting the convective flux, the flux of each ion in the $x-$direction can be calculated from Eq. (1) as,

$$\hat{\Gamma}_{\pm}(x) = -D\frac{d\hat{c}_{\pm}}{dx} \mp \frac{zFD}{RT}\hat{c}_{\pm}\frac{d\hat{\phi}}{dx} \tag{A1}$$

where $\wedge$ denotes the area-averaged quantity considering the width of the system to be unity. As it is observed that, until the first critical voltage, local electroneutrality is observed near both the anodic and the cathodic microchannel region ($\hat{c}_+ = \hat{c}_- = \hat{c}$), with linear concentration gradients observed at these regions, $\frac{d\hat{c}_+}{dx} = \frac{d\hat{c}_-}{dx} = \frac{d\hat{c}}{dx}$, the concentration gradient outside the nanochannel is given as,

$$\frac{d\hat{c}}{dx} = -\frac{\hat{\Gamma}_+ + \hat{\Gamma}_-}{2D} \tag{A2}$$

We neglect the concentration distribution in the quasi-equilibrium EDL region near the micro–nanochannel interface and consider the concentration of the ions to be zero at the interface of the micro–nanochannel (similar to the analogy of Levich's limiting-current density). Further, it is known that the concentration at the end of the source microchannel is equal to the bulk ionic concentration of the solution. Under these assumptions,

$$\hat{\Gamma}_+ + \hat{\Gamma}_- = -\frac{2Dc_0}{L_m} \tag{A3}$$

where L_m is the length of the microchannel (can also be taken to be equal to the length of the diffusion boundary layer). Considering $\bar{\Gamma} = -\frac{\hat{\Gamma}_+}{\hat{\Gamma}_-}$ to be the ratio of counter-ion and co-ion fluxes, we obtain the following expression for the limiting current density, $i_L = \left(\hat{\Gamma}_+ - \hat{\Gamma}_-\right)Fz$,

$$i_L = -\frac{2Dc_0Fz}{L_m}\left(\frac{\bar{\Gamma}+1}{\bar{\Gamma}-1}\right) \tag{A4}$$

It can be easily shown that, $\bar{\Gamma} = \frac{\hat{c}_{n+}}{\hat{c}_{n-}}$ [13,34], where $\hat{c}_{n+}$ and $\hat{c}_{n-}$ are the counter-ion and co-ion concentrations inside the nanochannel (averaged over the height of the nanochannel). The individual ionic concentrations inside the nanochannel can be approximately calculated using the Donnan equilibrium theory [35]

$$\hat{c}_{n\pm} = \pm\frac{\bar{c}}{2} + \sqrt{\left(\frac{\bar{c}}{2}\right)^2 + c_0^2} \tag{A5}$$

where $\bar{c} = \hat{c}_{n+} - \hat{c}_{n-} = -\frac{2\sigma_n}{FzH_n}$, is obtained from the electroneutrality condition inside the nanochannel. Substituting Eq. (A5) and the aforementioned conditions into Eq. (A4), we obtain the magnitude of the normalized limiting current ($I_L^* = |I_L/FzDc_0|$) per unit width at the end of the microchannel as,

$$I_L^* = \frac{2H_m}{L_m}\left(\frac{\hat{c}_{n+} + \hat{c}_{n-}}{\hat{c}_{n+} - \hat{c}_{n-}}\right) \tag{A6}$$

Using the limiting current expression, we now derive an expression to calculate the first critical voltage (V_{LI}), by considering the resistance of both nanochannel and microchannel, as both the resistances play an important role when the current deviates from the Ohmic region. We assume no significant voltage drop in the enrichment receiver microchannel and consider a linear voltage drop along the nanochannel and also along the depletion source microchannel. Under these assumptions, we first focus on calculating the voltage at the end of the nanochannel. Using Eq. (A1) and Eq. (4), and neglecting the diffusional flux, the limiting current (per unit width) along the $x-$direction for a symmetric monovalent electrolyte with equal diffusivities can be written as,

$$I_L = -\frac{F^2z^2DH_n}{RT}\frac{d\hat{\phi}}{dx}(\hat{c}_{n+} + \hat{c}_{n-}) \tag{A7}$$

Integrating both sides along the length of the nanochannel (from $x = x_s$ to $x = x_e$, where x_s is the coordinate where the nanochannel starts and x_e is the coordinate where the nanochannel ends) and substituting Eq. (A5), we obtain an expression for the voltage at the end of the nanochannel (averaged over the nanochannel height) as,

$$\hat{\phi}_N = -I_L\left(\frac{RTL_n}{F^2z^2DH_n(\hat{c}_{n+} + \hat{c}_{n-})}\right) \tag{A8}$$

We calculate the voltage at the end of the source microchannel, which is the desired first critical voltage (V_{LI}), by considering a linear voltage drop in the anodic depletion microchannel. Following the above procedure, and assuming, $\frac{d\hat{c}_+}{dx} = \frac{d\hat{c}_-}{dx} = \frac{d\hat{c}}{dx}$, the limiting current per unit width in the anodic microchannel can be written as,

$$I_L = -\frac{F^2z^2DH_m}{RT}\frac{d\hat{\phi}}{dx}(\hat{c}_+ + \hat{c}_-) \tag{A9}$$

It is important to note that the ion concentration varies linearly in the microchannel unlike the ionic concentration inside the nanochannel. Upon integrating the limiting current along the anodic microchannel and assuming the concentration of the ions to be zero at the anodic nanochannel–microchannel interface along with the aforementioned conditions

$$V_{LI} = \hat{\phi}_N - I_L\left(\frac{RTL_m}{F^2z^2DH_mc_0}\right) \tag{A10}$$

where $\hat{\phi}_N$ is the voltage (averaged over the nanochannel height) at the end of the nanochannel given by Eq. (A8). Substituting the dimensions of the geometry and all the system parameters used in the present simulation study, the magnitude of the normalized limiting current per unit width is 0.347, while the numerical solution is 0.3175. Further, the normalized first critical voltage ($V_{LI}^* = V_{LI}Fz/RT$) is 10.1225 and the numerical solution is 13.5394. The analytical expression slightly under-predicts the first critical voltage. This is because, we assumed that the concentration of the

ions is zero at the anodic micro–nanochannel interface. However, it is known from the detailed numerical simulations that there is a non-zero ionic concentration at this interface resulting in an interfacial jump in the potential. This jump in the potential can be obtained using the Donnan theory [35], by equating the chemical potential at this interface, provided the ionic concentration at this interface is known.

$$\hat{\phi}_N|_{x=x_{e^+}} - \hat{\phi}_N|_{x=x_{e^-}} = \frac{RT}{zF} ln\left(\frac{\hat{c}_+|_{x=x_{e^-}}}{\hat{c}_+|_{x=x_{e^+}}}\right) \tag{A11}$$

where $\hat{\phi}_N|_{x=x_{e^-}} (= \hat{\phi}_N)$ and $\hat{c}_+|_{x=x_{e^-}} (= \hat{c}_{n+})$ are the potential and cation concentration at the left end of the anodic micro–nanochannel interface (see Fig. A.1), which can be obtained using Eq. (A8), and Eq. (A5), respectively. Knowing the cation concentration at the right end of the micro–nanochannel interface, $\hat{c}_+|_{x=x_{e^+}}$, we obtain a modified expression for the first critical voltage.

$$V_{LI}|_{modified} = \hat{\phi}_N + \frac{RT}{zF} ln\left(\frac{\hat{c}_+|_{x=x_{e^-}}}{\hat{c}_+|_{x=x_{e^+}}}\right) - I_L\left(\frac{RTL_m}{F^2 z^2 D H_m c_0}\right) \tag{A12}$$

Note, the interfacial potential jump can also be obtained using the anion concentration at this interface by following the similar procedure. Upon substituting for $\hat{c}_+|_{x=x_{e^+}}$ from our numerical simulation, the modified normalized first critical voltage is found to be 13.8205, which compares reasonably well to the numerical simulation value.

References

[1] A. Hibara, T. Saito, H.-B. Kim, M. Tokeshi, T. Ooi, M. Nakao, T. Kitamori, Anal. Chem. 74 (2002) 6170.
[2] J.O. Tegenfeldt, C. Prinz, H. Cao, R.L. Huang, R.H. Austin, S.Y. Chou, E.C. Cox, J.C. Sturm, Anal. Bioanal. Chem. 378 (2004) 1678.
[3] A.L. Garcia, D.N.P.L.K. Ista, M.J. O'Brien, P. Bisong, A.A. Mammoli, S.R.J. Brueck, G.P. Lopez, Lab Chip 5 (2005) 1271.
[4] H.T. Hoang, H.D. Tong, I.M. Segers-Nolten, N.R. Tas, V. Subramaniam, M.C. Elwenspoek, J. Colloid Interface Sci. 367 (2012) 455.
[5] R. Qiao, N.R. Aluru, J. Chem. Phys. 118 (2003) 4692.
[6] X. Jin, S. Joseph, E.N. Gatimu, P.W. Bohn, N.R. Aluru, Langmuir 23 (2007) 13209.
[7] A. Mani, T.A. Zangle, J.G. Santiago, Langmuir 25 (2009) 3898.
[8] T. Postler, Z. Slouka, M. Svoboda, M. Přibyl, D. Šnita, J. Colloid Interface Sci. 320 (2008) 321.
[9] Y.S. Choi, S.J. Kim, J. Colloid Interface Sci. 333 (2009) 672.
[10] Q. Pu, J. Yun, H. Temkin, S. Liu, Nano Lett. 4 (2004) 1099.
[11] S.J. Kim, Y.-C. Wang, J.H. Lee, H. Jang, J. Han, Phys. Rev. Lett. 99 (2007) 044501.
[12] G. Yossifon, H.-C. Chang, Phys. Rev. Lett. 101 (2008) 254501.
[13] G. Yossifon, P. Mushenheim, Y.C. Chang, H.-C. Chang, Phys. Rev. E 79 (2009) 046305.
[14] R.F. Probstein, Physiochemical Hydrodynamics: An Introduction, John Wiley and Sons, Inc., New York, NY, 1994.
[15] A. Höltzel, U. Tallarek, J. Sep. Sci. 30 (2007) 1398.
[16] B. Zaltzman, I. Rubinstein, J. Fluid Mech. 579 (2007) 173.
[17] N.A. Mishchuk, Adv. Colloid Interface Sci. 160 (2010) 16.
[18] I. Rubinstein, Electrodiffusion of Ions, SIAM, Philadelphia, 1990.
[19] I. Rubinstein, E. Staude, O. Kedem, Desalination 69 (1988) 101.
[20] H. Daiguji, P. Yang, A. Majumdar, Nano Lett. 4 (2004) 137.
[21] H. Daiguji, P. Yang, A.J. Szeri, A. Majumdar, Nano Lett. 4 (2004) 2315.
[22] I. Rubinstein, B. Zaltzman, A. Futerman, V. Gitis, V. Nikonenko, Phys. Rev. E 79 (2009) 021506.
[23] R. Gross, J. Osterle, J. Chem. Phys. 49 (1968) 228.
[24] X.-L. Wang, T. Tsuru, S.-I. Nakao, S. Kimura, J. Membr. Sci. 103 (1995) 117.
[25] C.C. Chang, R.J. Yang, Microfluid. Nanofluid. 9 (2010) 225.
[26] V.G. Levich, Physicochemical Hydrodynamics, second ed., Prentice Hall, Inc., Englewood Cliffs, NJ, 1962.
[27] B. Hille, Ion Channels of Excitable Membranes, third ed., Sinauer Associates Inc., Sunderland, MA, 2001.
[28] V.V.R. Nandigana, N.R. Aluru, J. Fluids Eng-Trans. ASME. in press.
[29] V.V.R. Nandigana, Master's thesis, University of Illinois at Urbana-Champaign, 2011.
[30] http://www.openfoam.com/, 2011.
[31] E.F. Toro, Riemann Solvers and Numerical Methods for Fluid Dynamics, Springer-Verlag, 1999.
[32] H.K. Versteeg, W. Malalasekra, An Introduction to Computational Fluid Dynamics: The Finite Volume Method, second ed., Pearson Education Ltd., Essex, 2007.
[33] I. Rubinstein, L. Shtilman, J. Chem. Soc., Faraday Trans. 2 (75) (1979) 231.
[34] J.A. Manzanares, W.D. Murphy, S. Mafe, H. Reiss, J. Phys. Chem. 97 (1993) 8524.
[35] R.B. Schoch, J. Han, P. Renaud, Rev. Mod. Phys. 80 (2008) 839.